The XMaS beamline at ESRF: instrumental developments and high resolution diffraction studies

S. D. Brown,[a,c] L. Bouchenoire,[b,c] D. Bowyer,[d] J. Kervin,[a] D. Laundy,[e] M. J. Longfield,[a,c] D. Mannix,[a,c] D. F. Paul,[b,c] A. Stunault,[a,d] P. Thompson,[a,c] M. J. Cooper,[b] C. A. Lucas,[a] and W. G. Stirling[a,c]

[a]Department of Physics, University of Liverpool, Oxford Street, Liverpool L69 7ZE, UK, [b]Department of Physics, University of Warwick, Coventry CV4 7AL, UK, [c]European Synchrotron Radiation Facility, 6 Rue Jules Horowitz, BP 220, 38042 Grenoble, France, [d]Institut Laue Langevin, 6 Rue Jules Horowitz, BP 156, 38042 Grenoble, France, and [e]Daresbury Laboratory, Warrington WA4 4AD, UK.
Email: csmc@spec.warwick.ac.uk

The beamline, which is situated on a bending magnet at ESRF, comprises a unique combination of instrumentation for high-resolution and magnetic single-crystal diffraction. White-beam operation is possible, as well as focused and unfocused monochromatic modes. In addition to an eleven-axis Huber diffractometer, which facilitates simple operation in both vertical and horizontal scattering geometries, there is an in-vacuum polarisation analyser and slit system, mirrors for harmonic rejection, sub 4.2 K and 1 Tesla magnetic field sample environment, plus a diamond phase plate for polarisation conditioning. The instrumentation developed specifically for this beamline is described, and its use illustrated by recent scientific results.

Keywords: magnetism, diffraction, X-ray instrumentation.

1. Introduction

This beamline was originally conceived as a facility for the UK community interested in X-ray diffraction studies, especially of magnetic materials (the acronym XMaS stands for **X**-ray **Ma**gnetic **S**cattering). The objective was to build a simple, robust beamline with a single end station capable of providing a combination of flux and wave vector resolution that would facilitate high-quality diffraction studies of structural and magnetic scattering from single crystals, whilst also allowing the investigation of multilayers and thin films by means of grazing-incidence diffraction and reflectometry. In addition, ferromagnets would be studied by the white-beam technique (see Collins *et al*., 1992 and Zukowski *et al*., 1992).

The paper is structured as follows. After describing how the scientific objectives dictated the overall design (section 1.1), the detailed specification and operation of the beamline is discussed in sections 1.2 and 1.3. Section 2 deals with later instrumental developments, which have enhanced the experimental capabilities of XMaS. Finally, in section 3, examples of recent scientific investigations are presented: these have been chosen to illustrate the flexibility of the facility and the quality of the science possible with the unique combination of instrumentation on XMaS.

1.1 *Scientific objectives of the beamline*

The strong community interest in actinide magnetism, coupled with the phenomena of resonant X-ray scattering (RXMS, see Hannon *et al*., 1988) dictated that the flux of photons at actinide M-edge energies (~3–4 keV) needed to be optimised. With this in mind, the beamline was aligned on the "soft" sector of the BM28 bending magnet at the ESRF; this gives the emission spectrum a critical photon energy of ~10 keV. In order to limit attenuation of the incident X-ray beam at the lowest energies, the number and thickness of beryllium windows and air paths were minimised. The total thickness of Be in the incident beam is 0.85 mm.

The need for tunablity and reproducibility for RXMS studies led to a double-crystal fixed-exit monochromator design. The complexity of a variable-energy sagittally focusing monochromator was rejected in favour of a flat crystal design with the focusing needed to attain high flux in a small spot size, provided by a toroidal mirror. The toroidal mirror, which is the second optical element, provides 1:1 focusing and is uncooled. The original optical design options were discussed by Paul *et al*. (1995). In order to allow studies of ferromagnets, using circularly polarised radiation, unfocused white beam is provided for. This facility was exploited at an early stage of construction (Laundy *et al*., 1998). The diffractometer can be used with focused or unfocused beam, the latter providing higher wave vector resolution. Both horizontal and vertical scattering geometries are readily available.

Figure 1
The optics of the XMaS beamline. Details as described in the text.

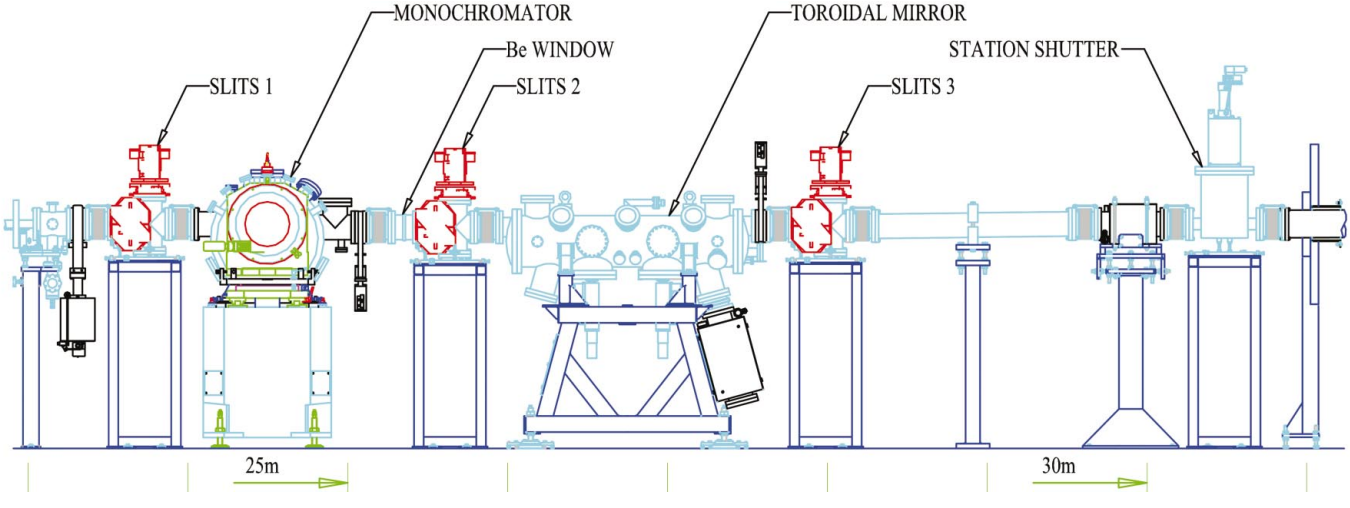

1.2 *Specification of the beamline*

The optical elements are as shown in the schematic diagram in Fig. 1. On the XMaS beamline the monochromator is the first optical element. It is situated 24.5 m from the source point and is water-cooled. To attain high precision and reproducibility (~0.0001°) the goniometer is driven by a DC servo motor; this is essential for the energy scanning required for RXMS investigations. The first crystal, which is an ESRF design, intercepts the full vertical fan of radiation and is water-cooled through a series of galleries close to the diffracting surface and parallel to the beam direction. The second crystal is kinematically mounted in a crystal "cage" (an in-house design) and is positioned by three linear actuators which are driven by encoded stepper motors; this provides a constant exit height.

The Zeiss focusing mirror (length 1200 mm, width 120 mm) was machined from single crystal silicon to a cylindrical cross section of radius 116 mm. It is bent pneumatically to a toroidal form of radius 5.5 km and is situated 26 m from the source point to provide 1:1 focusing at the sample position. The mirror is rhodium-coated, and is set at a grazing incidence angle of 4.5 mrad, leading to an upper energy cut-off ~15 keV.

The layout of the equipment in the experimental hutch is shown schematically in Fig. 2. The upper beam pipe carries the focused monochromatic beam which is inclined at 9 mrad to the horizontal, while the lower horizontal beam pipe delivers white or unfocused monochromatic beam. The vessel, which is at 49 m from the source, contains two mirrors for harmonic rejection (see section 2.1). A particular feature of the beam delivery system is the modular assembly of attenuators, beam monitors and in-vacuum slits, situated 50 m from the source. These modules can be placed in any sequence and are interchangeable between upper and lower beam paths. The phase plate assembly (see section 2.2) can be used to manipulate the polarisation of the beam incident upon the sample. It is positioned immediately before the telescopic vacuum flight path, which minimises the air path of the incident beam.

The measured flux of monochromatic focused radiation at the sample position is shown in Fig. 3, normalised to 0.1% bandwidth. These data are in good agreement with the predicted flux figures within the accuracy of the model's assumptions, *e.g.* for mirror roughness. The actual flux at the sample position depends on the slit widths used to limit the primary divergence and varies from experiment to experiment. Typically, with full illumination of the monochromator, $\Delta E/E$ varies from 1×10^{-4} at 3 keV to 3×10^{-4} at 15 keV. Thus the maximum flux at the sample position at, say, 10 keV is ~5×10^{12} ps^{-1} in a focal spot size of 0.8 mm vertical by 0.3 mm horizontal. The Huber diffractometer provides four-circle capability in both vertical and horizontal scattering geometries. The sample circles are aligned within a sphere error of less than 30 μm and the detector circles within 60 μm. The circles are driven though 20:1 reduction gear boxes. The diffractometer is mounted on a table with transverse and vertical translations, the latter allowing movement between the two incident beam positions.

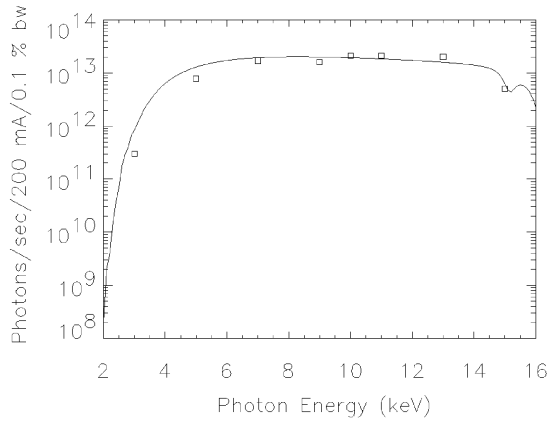

Figure 3
The measured monochromatic flux at the sample position, □ compared to the predicted values (continuous line) for an operating current of 200 mA.

When focused monochromatic beam is used the table can also be tilted to 9 mrad in alignment with the incident beam. The detector arm accommodates a conventional and an evacuable polarisation analyser; the latter being described in section 2.3. In addition to a standard sample goniometer the Φ circle can hold a conventional displex cryostat with base temperature ~10 K and a specially adapted one, capable of temperatures below 2 K (see section 2.6); all can be located on a motorised precision XYZ mount (section 2.5). A 1.6 Tesla electromagnet can provide fields parallel and perpendicular to the incident beam (section 2.6).

Figure 2
Beam conditioning in the experimental hutch

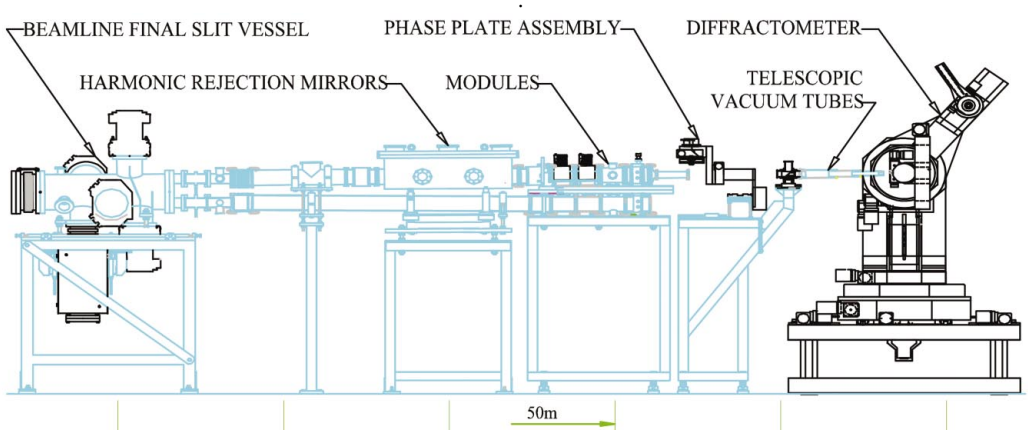

1.3 *Operation of the beamline*

The XMaS facility became available for users in April 1998. The ESRF provides approximately 200 days per year of user beam, mainly in "continuous" or "2/3rds" fill modes that produce the maximum circulating current of 200 mA; in addition 16 bunch (90 mA) and single bunch (10 mA) modes are also available for some 25% and 10% of the user beamtime, respectively. Beam lifetimes are generally greater than 40 hrs and two refills per day are the norm. Typically the storage ring operates for 6 days per week and most of the investigations on XMaS require a full 6 day period. Thus, when allowance has been made for commissioning, maintenance, repairs *etc*. approximately 30 experiments per year are carried out. The majority of experiments (~65%) are performed with focused monochromatic radiation on single crystals and exploit the full angular capabilities of the diffractometer.

Approximately 30% of the experiments use grazing incidence X-ray diffraction or reflectometry to study multilayers, thin films and surfaces. Here the capability of the instrument to operate alternately in vertical and azimuthal scattering geometries with minimal downtime is critical. A minority of the beamtime (~5%) uses the white beam together with a magnetic field sample environment and it takes approximately 1 day to switch to this mode of operation.

2. Instrumental developments

2.1 *Mirrors for harmonic rejection*

Initial measurements performed at relatively low energies of the uranium M_V and M_{IV} edges (at 3.55keV and 3.73keV, respectively) proved problematic due to harmonic contamination from the monochromator, exacerbated by preferential absorption of the Si (111) reflection in the beryllium windows compared to the (333) and (444) harmonic reflections. A double mirror harmonic rejection assembly was designed and installed to overcome this problem. The pyrex mirrors are Pd-coated over half their width to cover the energy range 6–15 keV, no coating is necessary at lower energies. The angular range is 4–7 mrad.

Fig. 4 compares the best harmonic rejection that could be achieved by de-tuning the monochromator (upper diagram) and the performance using the harmonic-rejection mirror assembly (lower diagram). The large harmonic contamination, although removable with use of a single channel analyser, still contributes to the dead-time of the detector, as is apparent from the flat topped peak in (a). The single channel analyser confirmed that, within experimental error, the measured signal in (b) is solely due to the fundamental wavelength.

2.2 *Phase plate for polarisation conditioning*

The incident linear polarised radiation can be converted into circular polarisation (P_C) either from X-rays emitted above/below the electron orbit or using a quarter phase plate. The latter technique is the only way to look at highly anisotropic magnetic materials for which the direction of the sample magnetisation cannot be reversed. The phase plate assembly is situated upstream of the diffractometer. The diamond crystal is mounted on a Huber goniometer and is driven to the quarter wave plate conditions, for maximum P_C, with a θ and a χ circle. The former rotation stage, which moves the crystal off the Bragg condition, has an accuracy of 10^{-4} degrees (0.36 arcseconds). It is orthogonally mounted on the χ circle. The χ circle sets the optical axis of the diamond at 45° to the incident and plane polarization, with an accuracy of ±10 arcseconds. A counter balance was also mounted onto the arm of the χ circle. These two circles are positioned upon two translation stages giving horizontal and vertical adjustment

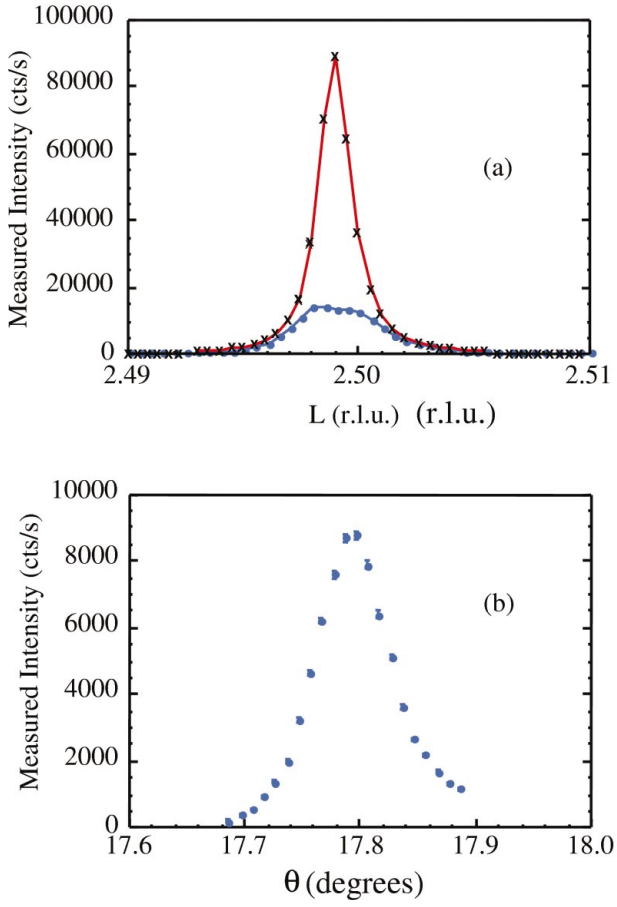

Figure 4
The need for harmonic rejection: In (a) the upper line represents the total signal into the detector when the 0 0 2.5 satellite of $UAs_{0.8}$ $Se_{0.2}$ is studied at 3.728 keV. The lower line is the actual signal when the second crystal of the monochromator is detuned to give some harmonic rejection. The dominant contribution to the total signal still comes from $\lambda/4$ contamination. (b) The true energy signal selected by the harmonic rejection mirrors.

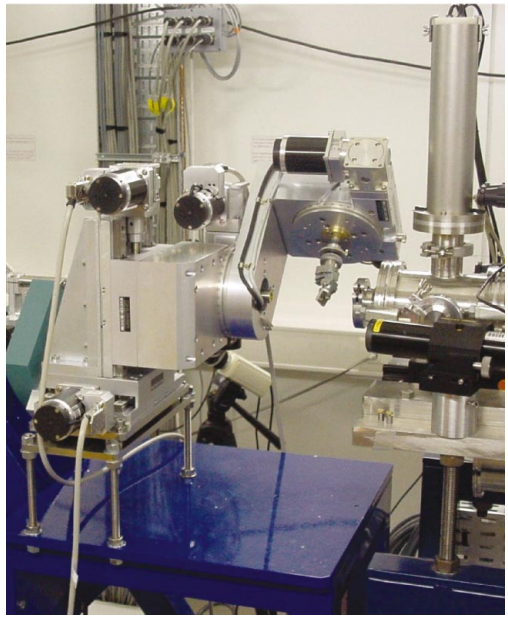

Figure 5
The diamond phase plate assembly.

within 10 μm. All the motors are controlled from SPEC software, which is also used elsewhere on the beamline. The θ circle has an encoder installed.

Fig. 6 shows the possible values of $P_C = \pm\sqrt{(1-P^2_1-P^2_2-P^2_{un})}$ deduced from our polarisation analyser data (dots), P_{un} being the unpolarised component at 7.833 keV. The 0.78 mm thick diamond crystal was operated in Laue transmission using the (11-1) diffracting planes which make a 19.47° angle with the [111] direction normal to the phase plate surface. At this energy, the diamond converted the 99.87(±1)% linearly polarised incident beam into 99.85(±1)% circularly polarised X-rays. The high accuracy of these figures derives from the fact that it is *(1-P)* that is measured by scattering in the orbital plane at 90º. For this test measurement the beamline divergence was restricted to 1 arcsec and the model is convoluted with a Gaussian function of this width.

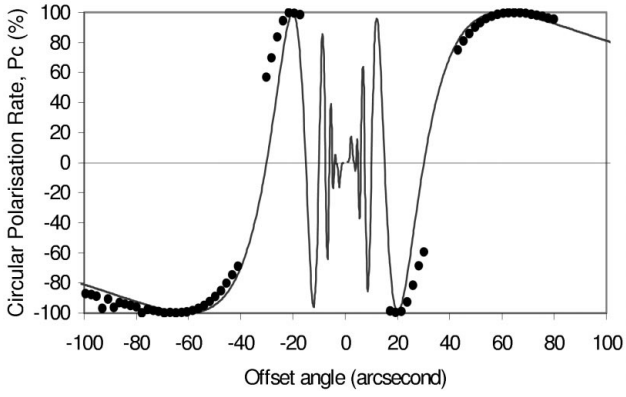

Figure 6
Circular polarisation of the beam conditioned by the diamond phase plate (•) compared to the modelled polarisation (solid line), as a function of the off-set from the Bragg angle.

2.3 *Polarisation analyser*

The three-axis XMaS polarisation analyser, pictured schematically in Fig. 7, has been designed to facilitate the study of changes in the polarisations of the X-ray beam after diffraction from the sample. The in-vacuum design allows the device to be used at low energies (~3 keV) which is particularly useful, for example, in experiments performed at uranium M-edges. The θ axis allows alignment of the analyser crystal to a diffracting condition, with θ_{Bragg} at, or close to, 45°. The second rotation axis allows rotation of the diffracting plane of the analyser crystal about the beam. Any component of the incident polarisation lying in the diffracting plane will go to zero on charge scattering for $\theta_{Bragg} = 45°$.

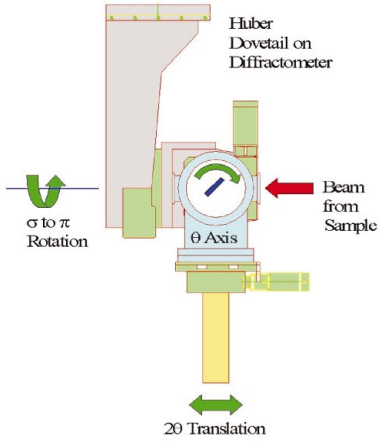

Figure 7
Schematic diagram of the thee-axis in-vacuum polarisation analyser.

The third linear axis allows translation of the detector in a 2θ geometry in order to track the diffracted beam. Conventionally, for vertical scattering experiments, the incident polarisation is referred to as σ polarised and any component orthogonal to it (*i.e.* vertically polarised) as π polarised. Thus, by positioning the rotation about the beam such that the diffracting plane of the analysing crystal is vertical, one is sensitive only to the σ polarised component and conversely a horizontal analyser crystal diffraction plane measures the π component.

2.4 *In-vacuum tube slits*

These slits were developed in order to define the incident or outgoing beam at a position very close to the sample. The design adopted satisfies three basic requirements, which are to define a footprint on a sample, to reduce background scatter and to enable isolation of small regions of interest on the sample. The assembly may equally well be mounted on the incident or diffracted beam path. In order to avoid possible collisions with the diffractometer, all of the actuation mechanics are spatially separated from the sample position, with the four independent slit jaws positioned by a system of levers as shown in Fig. 8. The maximum overall opening aperture of the

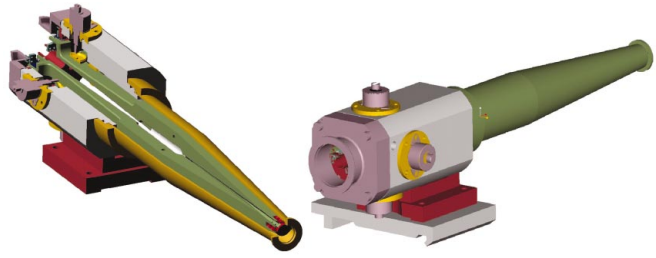

Figure 8
Schematic picture of the in-vacuum tube slits. The left hand cut-away diagram shows the lever arm actuator mechanism.

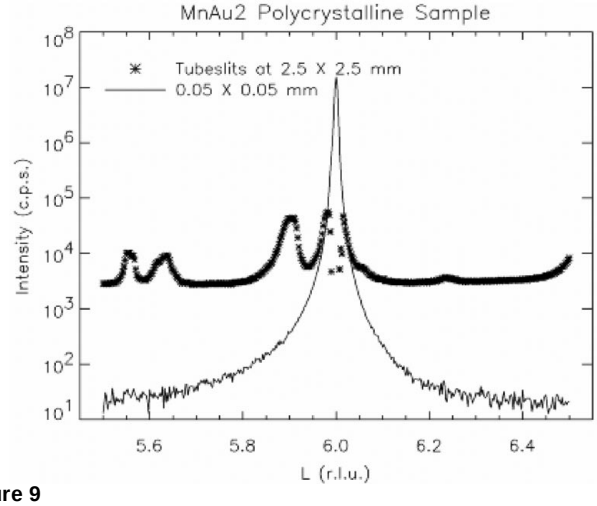

Figure 9
Use of the tube slits to select a single crystallite in a $MnAu_2$ powder. High background (10^3 cps) is evident in the powder peak (points **x x**) obtained with the slits wide open. [NB No attenuators were used in this scan, hence the suppression of the peak at 6 r.l.u. at count rates ~10^5cps due to detector saturation.] When the slits are narrowed down to select one crystallite (lower trace - continuous line), the background is removed and a dynamic range of six decades was recorded with attenuators.

slit assembly is 4 mm x 4 mm and each jaw can be independently positioned to micron precision. The slit assembly may be mounted on X-95 compatible optical rail and is therefore interchangeable with other beamline modular components. Motion is provided to the levers through in-house designed miniature linear vacuum feed-throughs with limit switches fitted on all translations.

The value of the use of the tube slits is shown in Fig. 9. The upper line shows the "powder" pattern obtained from a sample of $MnAu_2$ with the slits wide open. The general background is ~$5x10^3$ cps. When the slits are closed down to 50 μm x 50 μm one single crystallite is illuminated and the signal is six orders of magnitude above background. The count rates (up to 10^7 cps) are still sufficient for single crystal studies of material that is only available in "polycrystalline" form.

2.5 *Precision sample mount*

A new motorised mounting system for the APD cryostat has been designed to fit into the Huber 410 Φ circle, as shown in Fig. 10. The present mount utilises dovetail linear slides for the X and Y translations, driven by manually adjusted screw threads. The Z translation consists of a sleeve and cylinder linear guide adjusted by a large threaded ring. These slides and the way that they are adjusted makes precise and reproducible movements very difficult to obtain. Since these adjustments are usually not motorised, many hours of useful beamtime can be lost trying to find a "sweet spot" on a crystalline sample. Also, problems are encountered with this type of mount whilst tightening the screws to lock these translations in place. During cooling the cryostat contracts, sometimes by more than 0.5 mm and sample alignment afterwards is very difficult. However, once the cryostat is fixed in place it is very stable.

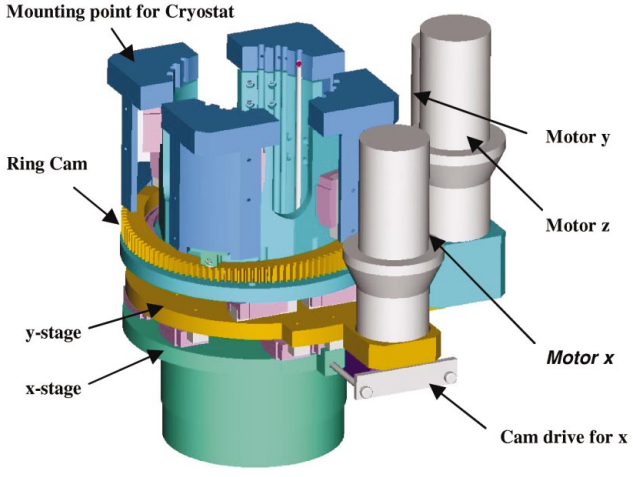

Figure 10
The motorised XYZ mount.

The new mount fixes to the diffractometer in exactly the same manner as the Huber design and has the same translation limits. The three linear translations (X, Y and Z) are mounted onto high precision linear bearings. The independent X and Y movements are obtained by mounting a cam onto the shaft of a stepper motor with a 100:1 harmonic drive gearbox to minimise backlash. This cam is mounted within two linear bearings, thus allowing movement perpendicular to the axis of the motor (X and Y) with a minimum of backlash. The Z translation is guided by high precision linear bearings and driven by a stepper motor with a 100:1 harmonic drive gearbox *via* a large toothed ring cam. The cryostat and Z stage are mounted upon cam followers and as the large toothed cam turns this provides the Z translation. This stage is held in place on the cam by eight strong springs. Calculations indicate that this combination should provide the resolution and rigidity required for the XMaS diffractometer.

2.6 *Sample environment*

2.6.1 *Magnetic field* The magnet at the XMaS beamline, supported from the base of the Huber diffractometer, fits within the Eulerian cradle as shown in Fig. 11. The geometry allows the magnet to be oriented in one of two positions 90° apart, about the vertical axis. Thus both transverse and longitudinal fields may be applied, allowing the separation of spin and orbital contributions to magnetic scattering signals. The geometry of the yoke allows for the maximum number of field turns within the geometrical constraints of the diffractometer. With a further mounting position it is possible to provide a vertical field if required. It can deliver a field of 1.0 T in an air gap of 50 mm. To achieve this with a magnet of manageable size, water-cooled hollow conductors have been used for the coils. A magnetically efficient yoke configuration occupies the lower half of the vertical scattering plane, leaving the other half open for the cryostat and scattered beam. The yoke and poles have been manufactured from ARMCO grade iron. The gap set at 50 mm, the homogeneity of the field in the middle of the gap in a co-axial cylinder, a = 5 mm, r = 2.5 mm is within 2% of the central value. Conical pole tips can be mounted on the adjustable poles and, with a 2.5 mm gap, a field of 1.5 T is achievable at a current of 250 amps.

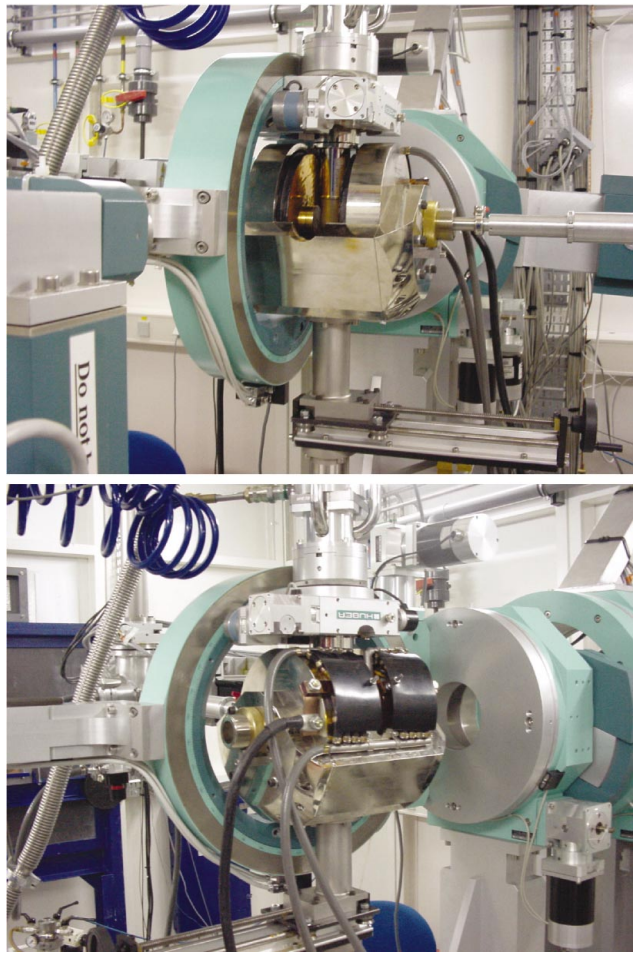

Figure 11
The 1–1.5 T electromagnet, which fits inside the chi circle, shown with the field parallel to the incident and scattered beams in the upper and lower pictures, respectively.

2.6.2 *Low-temperature displex cryostat* In addition to a commercial standard two-stage displex cryostat, which operates down to ~10 K and mounts on the chi circle of the diffractometer, a specially adapted three-stage displex capable of sample temperatures down to 1.7 K is in routine use. This novel device, which is being developed by the cryogenics Laboratory at Institut Laue Langevin, Grenoble, may be operated over a wide range of angles without degradation of base temperature. The three-stage device is ~40 mm longer than a standard displex and requires little adaptation of the mount to fit it onto the chi circle. An example of its use is given in section 3.1.

2.7 *The diffractometer*

The 11-axis Huber diffractometer is depicted in Fig. 2. The vertical translation exists to permit alignment of the sample to the three possible beam positions: white unfocused; monochromatic unfocused (both at –20 mm); monochromatic focused (at +225 mm). Since the mirror deflects the monochromatic beam upwards through 9 mrad, the facility to tilt (±1 deg) is provided in order to maintain orthogonality between the focused beam path and all horizontal circle axes. A horizontal translation (z) is present to facilitate sample alignment. The eight circles have a resolution of 1 arcsec and absolute accuracy of 20–30 arcsecs. The sphere of confusion is 30 μm with unsupported loads up to 10kg. With the use of SPEC software, orientation matrices may be defined in either vertical or horizontal four-circle scattering geometries. In either of these geometries the two out-of-scattering-plane circles may still be driven. It is equipped with a conventional Huber analyser, which carries a small analyser crystal goniometer head. The in-vacuum polarisation analyser stage has been described in section 2.3

3. Science on the beamline

The flexibility of the XMaS beamline allows a wide range of experiments to be performed. The major interest lies in magnetism and magnetic scattering, but, also, the beamline is well suited for studies of thin films and surfaces. In addition, some materials science studies are performed. Below, examples of some recent results from these scientific areas are highlighted.

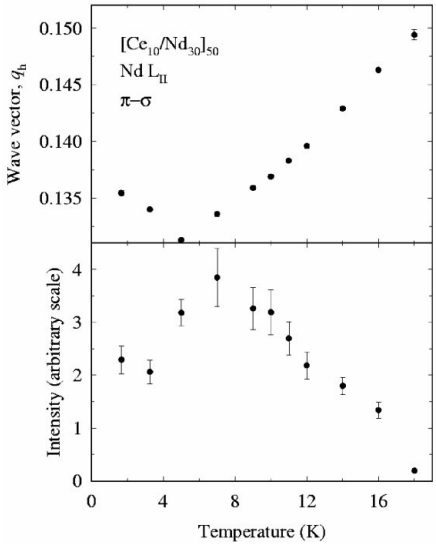

Figure 12
The temperature dependence of the ordering wave vector q_h (upper panel) and integrated intensity (lower panel) of the magnetic reflection at Q = (q_h, q_k, 3) for the $[Ce_{10}Nd_{30}]_{50}$ superlattice (Lee *et al*., 2001; see section 3.1.1).

3.1 *Magnetism*

3.1.1 *Magnetic thin films* The growth of single-crystal Ce/Nd superlattices using MBE allows the complex magnetic interactions between the different constituents of the superlattice and the inequivalent sites of the DHCP structure to be studied (see Goff *et al*., 1999). The high signal-to-background and narrow *Q*-resolution make X-ray magnetic resonant scattering (XMRS) ideal to investigate incommensurate magnetic ordering in thin-film samples. For a superlattice of composition $[Ce_{10}Nd_{30}]_{50}$, ordering of the Nd hexagonal moments is detected below $T_N \sim 18$ K with a sinusoidal modulation in the basal plane and an antiferromagnetic coupling between adjacent hexagonal planes. However, in contrast to bulk Nd, these sites remain in a transverse 2-*q* magnetic structure down to the base temperature $T \sim 1.7$ K, and the antiferromagnetic ordering on the cubic sites is suppressed. Fig. 12 shows abrupt changes in the intensity and ordering wave vector below $T \sim 6$ K, as a function of temperature. It is correlated with the onset of *c*-axis ferromagnetic ordering on the cubic sites determined in complementary neutron studies. The top panel shows the change in the magnetic modulation and the lower panel shows the change in the antiferromagnetic order parameter. The decrease in intensity at low temperature reflects the transfer of magnetic scattering intensity to the ferromagnetic component of the magnetic structure. The effect of the epitaxial strain in the Nd blocks is, therefore, related to the application of pressure to bulk samples. This superlattice forms a coherent magnetic structure, and further XMRS studies are planned to determine the magnetic ordering and electronic state of the Ce.

3.1.2 *Lanthanide magnetism* The spatial ordering of higher-order multipoles of the lanthanide and actinide *f*-electron wavefunctions can be investigated directly by resonant X-ray scattering: neutrons do not directly couple to these *f*-electron quadrupolar interactions and so can only provide direct information on the magnetic dipolar ordering. $TmGa_3$ undergoes a first-order phase transition to an anti-ferroquadrupolar structure below $T_Q = 4.29$ K, slightly before the onset of antiferromagnetism at $T_N = 3.26$ K. (Czopnik *et al.*, 1985; Morin *et al*., 1987). We have investigated these two phases using X-ray resonant scattering at XMaS. The antiferroquadrupolar order and antiferromagnetism occur at the same propagation wavevector q = (0 ½ ½); however, the scattering from magnetic dipoles and electric quadrupoles can be separated using polarisation analysis. The resonant scattering at the (0 0.5 1.5) position for $\sigma\sigma$ (lower panel) and $\sigma\pi$ (middle panel), in the vicinity of the Tm L_3 absorption edge, is shown in Fig. 13. The circles in the top panel are the absorption coefficients taken from the measured fluorescence. Since dipole resonant X-ray magnetic scattering is forbidden in the $\sigma\sigma$ channel, the observation of such scattering arises purely from the antiferroquadrupolar ordering.

The temperature dependence of the dipole resonance of the $\sigma\sigma$ and $\sigma\pi$ intensities are compared in Figure 14. From the temperature dependence we ascribe the $\sigma\pi$ scattering as arising predominately from the magnetic order and the $\sigma\sigma$ from the antiferroquadrupolar order. The difference in the temperature dependence suggests that quadrupole ordering is driving the ordering of the magnetism. Furthermore, the widths, in reciprocal space, of the magnetic $\sigma\pi$ scattering peaks are much greater than those of the antiferroquadrupole $\sigma\sigma$ scattering peaks which also suggests that the antiferroquadrupole interactions frustrate the long range ordering of the magnetism in this system. This study exploited fully the unique combination of instrumental facilities available on XMaS (sub 4.2 K temperature, azimuthal scattering geometry, polarisation analysis, magnetic field *etc*.). Further measurements are planned at XMaS on the study of this fascinating interplay of ordering in $TmGa_3$.

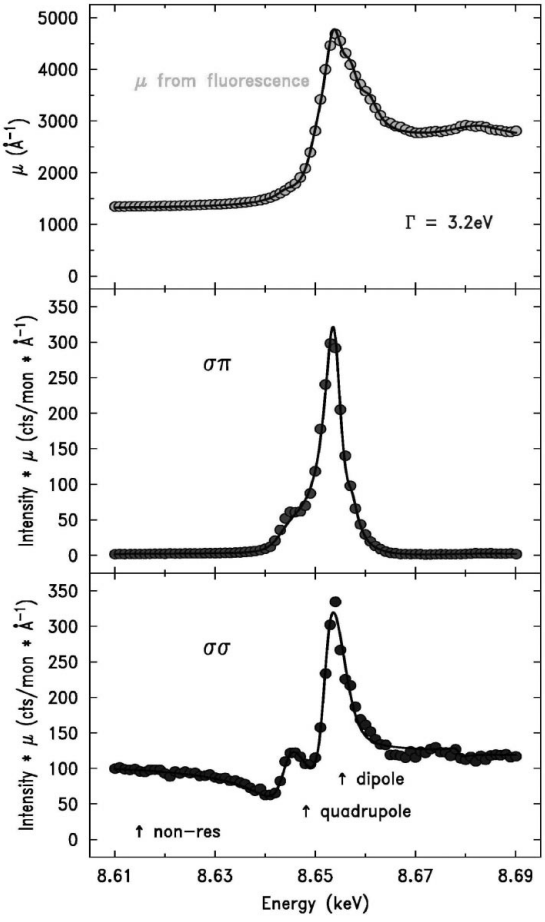

Figure 13
Energy dependence of resonant scattering from $TmGa_3$,, as described in the text.

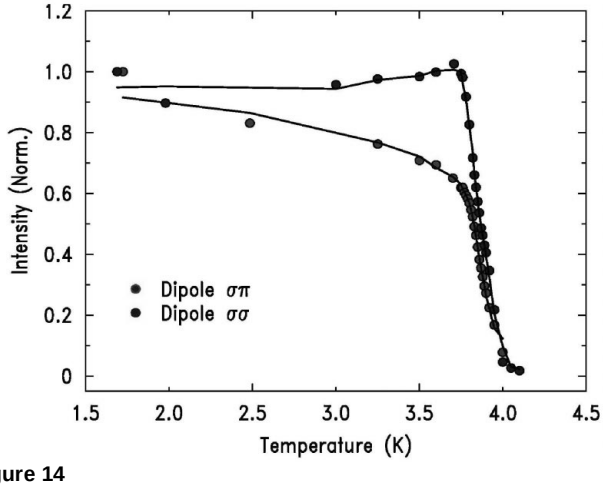

Figure 14
Temperature dependence of dipole resonant scattering from $TmGa_3$. The upper and lower data sets are the σσ and σπ scattering channels, respectively, separated by polarisation analysis.

3.1.3 *White beam studies of ferromagnets* Heusler alloys are interesting magnetic systems because they possess ferromagnetic order even though their constituent elements are not bulk ferromagnets. The localised moments are associated with the *3d* electrons. Previous neutron diffraction studies (Rakhecha *et al*., 1976) predicted a delocalised spin moment aligned parallel to the Mn *3d* moment although magnetic Compton scattering data (Zukowski *et al*., 1997) showed an antiparallel polarisation. This X-ray diffraction study was performed in order to test the ability of the KKR calculation to describe the high-order magnetic form factors, since the conduction electron delocalised moments are difficult to infer from form factor data. The experimental technique uses the suppression of charge scattering at 90º in the orbital plane of the synchrotron to maximise the ratio of magnetic to charge scattering. In fact the experiment is carried out with the white beam extracted at an angle between 2 μrad and 10 μrad above or below the orbital plane and the energy-sensitive detector at 90º horizontally (Laundy *et al*., 1998). The magnetic field is aligned alternately parallel and anti-parallel to the incident beam direction. In that case the ratio, *R*, of the magnetic form factor $f(K)_M$ to the charge form factor $f(K)_C$ is measured.

$$R = \left(\frac{E}{mc^2}\right)\frac{f(K)_M}{f(K)_C}\frac{P_C}{1-P_L}$$

where E is the photon energy and P_C and P_L are the degree of circular and linear polarisation, respectively. This equation shows that the higher-order reflections, which will occur at higher photon energies, are enhanced by the factor E/mc^2, neutron data only extend typically to 1 $Å^{-1}$. Fig. 15 shows that the X-ray data at small momentum transfer are in agreement with both the neutron data and the KKR calculation but there is a tendency for the higher-order reflections, that sample the magnetisation density near the core, to deviate from the modelled values. Full analysis of these data will appear elsewhere.

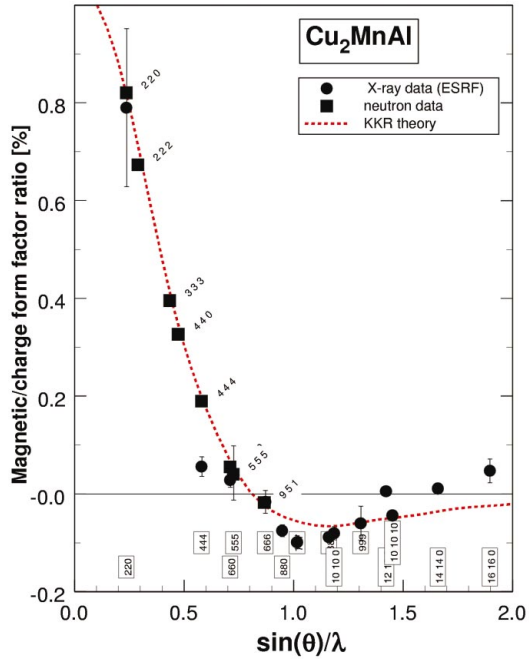

Figure 15
Comparison of the magnetic form factor of the Heusler alloy, Cu_2MnAl, as measured in the present X-ray study (•) and by neutron diffraction (■) (Rakhecha *et al*., 1976). The red line is the predicted form factor calculated according to the KKR-CPA method (Kaprzyk: unpublished). The values of the momentum transfer sin(θ)/ λ are expressed in $Å^{-1}$.

3.1.4 *Actinide magnetism* High-resolution studies of lattice behaviour can be a valuable complement to direct *magnetic* scattering

measurements. The magnetic properties of the *5f* actinides are especially interesting, presenting aspects similar to the *4f* lanthanides and *3d* transition metals. Detailed studies of the NaCl-structure UX compounds, where X is either a pnictide or chalcogenide, have demonstrated a wide range of spin structures and phase transitions. A recent investigation of the $U(As_{1-X}\ Se_X)$ solid solutions (Longfield *et al.*, 2001) used the XMaS instrument to study magnetostriction in the antiferromagnetic phase. As shown in Fig. 16, the (006) charge-scattering Bragg peak of an x = 0.18 sample splits at the transition (~60 K) to the low-temperature (tetragonal) incommensurate phase. At 12 K the tetragonal distortion $(c\text{-}a)/c = 2.3\text{x}10^{-4}$. Such studies of lattice distortions accompanying changes in magnetic ordering provide extremely valuable information, but require very good wave vector resolution. To achieve the results of Fig. 16, with an X-ray energy of 8 keV, a Ge (111) analyser was required, with the incident vertical beam size reduced to 40 μm.

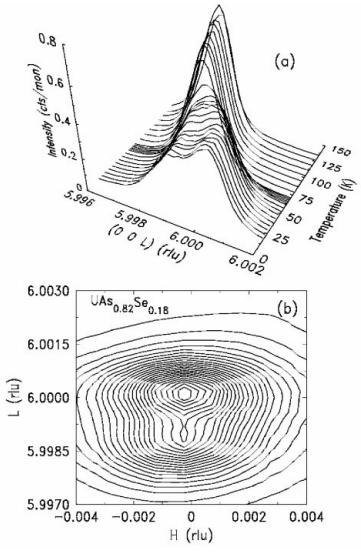

Figure 16
Magnetically induced splitting of the (006) Bragg peak in $U(As_{0.82}\ Se_{0.18})$. The upper diagram shows the temperature evolution.

3.2 *Thin film, surfaces and electrochemistry.*

The XMaS beamline is well suited to a variety of surface X-ray scattering experiments, especially as the diffractometer can accommodate different sample environments whilst retaining a flexible scattering geometry. For example, the temperature-dependent ordering of gold nanoparticles evaporated onto silicon substrates has been studied by grazing-incidence X-ray scattering and key differences in the in-plane and out-of-plane ordering have been identified (Nicklin *et al.*, 2001). Similar measurements on semi-crystalline polymer films on silicon have identified new surface effects, such as faster kinetics and preferred orientation, that were not predicted from the known bulk polymer behaviour (Kawana *et al.*, 2001).

3.2.1 *Surface electrochemistry* Several experiments on surfaces in an electrochemical environment have also been performed. Fig. 17 shows a schematic of the electrochemical cell, which was used for these experiments. The surface under study (*e.g.* single crystal Au, Pt or Ni) forms the working electrode of a 3-electrode cell designed so that the sample surface forms the highest point and is thus accessible to the incident X-ray beam. The surface is contained within a liquid environment by a reservoir of electrolyte trapped by a thin polypropylene film. This cell fits into the Huber goniometer on the beamline and permits both high-angle diffraction and low-angle reflectivity studies of the crystal surface under electrostatic potential control. Fig. 18 shows some representative results for a Au (111) surface in acid solution containing Ni cations. The main part of the figure shows reciprocal space scans along the <1 1 0> direction through the (1, 0, 0.2) reciprocal lattice point made at two electrode potentials, 0.35 V, where the surface is unreconstructed, and –1.0 V, where Ni has been electrodeposited onto the surface and incorporated into the Au-(23 x √3) surface reconstruction (Wang *et al.*, 1992). At 0.35 V the scan shows only a single peak due to the Au (1, 0, *l*) crystal truncation rod [CTR]. Stepping the potential to –1.0 V causes a decrease in intensity at the CTR position and the appearance of another peak due to one of the three rotational domains of the (23 x √3) reconstructed phase. By monitoring the kinetics associated with the growth of the reconstruction peak it is apparent that, in addition to the reconstruction of the Au surface, Ni is also incorporated into the surface reconstruction. This is in agreement with previous STM experiments (Moller *et al.*, 1996). At sufficiently negative potentials a thin Ni film can be deposited onto the Au surface and it has been shown that the (23 x √3) mixed Ni–Au adlayer forms the transition between the Au (111) lattice and the overlying Ni (111) film. This is confirmed by energy-dependent surface X-ray diffraction results, illustrated in the inset to Fig. 18. The X-ray intensity at the (1, 0, 0.2) CTR position is constant as the incident X-ray intensity is scanned through the Ni K adsorption edge (8.33 keV). As shown in the inset to Fig. 2, however, the intensity at the (1.022, 0.022, 0.2) position (the reconstruction peak) shows a clear dependence on the incident X-ray energy, consistent with the presence of Ni in the interface adlayer.

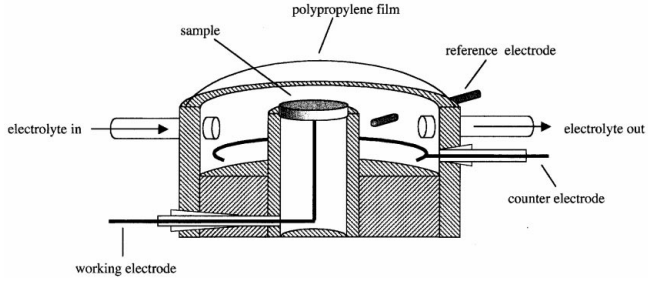

Figure 17
A sectional view through the electrochemical X-ray scattering cell. For the experiments described, the solution was a modified Watts bath containing Ni cations and the sample was Au (111).

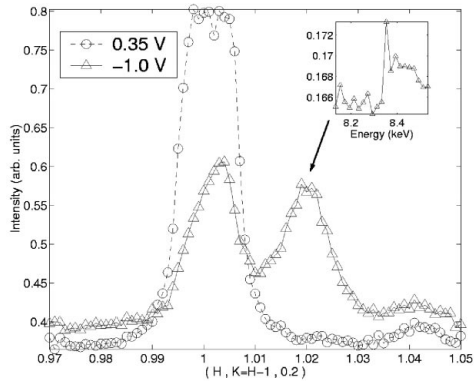

Figure 18
Reciprocal space scans along the <1 1 0> direction through the (1, 0, 0.2) CTR position. At –1.0 V the second peak arises due to the (23 x √3) reconstruction of the Au(111) surface. The inset shows a scan of the incident X-ray energy at a fixed reciprocal lattice point, (1.022, 0.022, 0.2), shows the peak due to the reconstructed phase. The changes indicate that Ni is incorporated into the Au surface reconstruction.

These results can be extended to study phenomena such as surface oxidation and catalytic reactivity, *in situ*, as the surface reaction can be carefully controlled by the solution species and/or the applied electric potential at the interface.

3.3 *Materials science*

3.3.1 *Stacking faults in cobalt alloy films* Crystallographic defects in polycrystalline Co-alloy thin films, which may be used as magnetic recording media, have been studied on XMaS (Holloway *et al*., 2001). The structure of the films is such that the underlayers mask the Co diffraction peaks necessary for the analysis of crystallographic defects; therefore grazing-incidence X-ray scattering (GIXS) was used to restrict the X-ray penetration depth to the Co-alloy layer which is typically between 100 Å and 250 Å. Since the defects of interest occur in the plane of the film the in-plane diffraction data were fitted to quantify the level of stacking faults. This was possible to an accuracy of 1% using high-resolution XMaS data. Fig. 19 shows GIXS scans for two films with different growth textures of the Co-alloy. An overall estimation of the amount of film in an fcc-like environment can be obtained by fitting the data, *e.g.* 13% ± 1% for the 1120 film (upper data set) and 8% ± 1% for the 1010 film (lower data set). In each case the stacking model produces the excellent straight-line fit to the data sets. These results lead to a quantitative assessment of the effect of stacking faults on the magnetisation reversal) provide a fundamental understanding of the underpinning role of magnetocrystalline anisotropy in the magnetisation reversal in Co-based thin films (Holloway & Laidler, 2000) and in determining the origins of time-dependent magnetisation in these technologically important materials (Weller & Doerner, 2000).

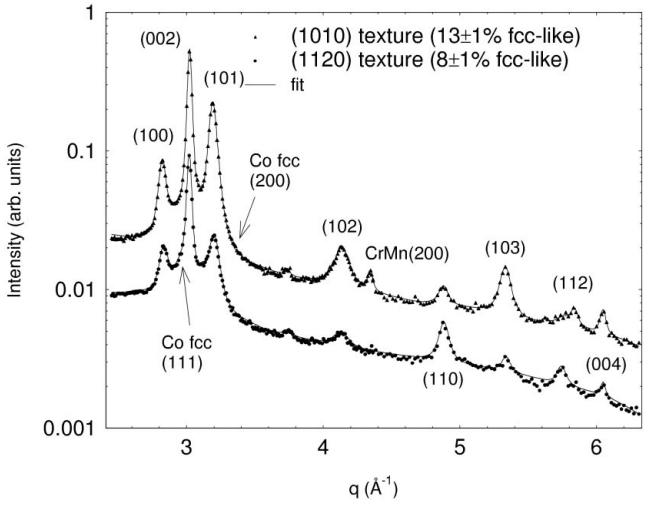

Figure 19
GIXS data for two Co-alloy thin films with different growth textures of the Co-alloy. The upper and lower curves are stacking model fits to the data for 1120 and 1010 films, respectively. The stacking fault pattern is analysed in terms of the percentage of the alloy with an fcc-like environment in each phase. [Taken from Holloway *et al.* (2001).]

3.3.2 *Electroluminescent polymers* Electroluminescence from organic ultrathin layers has been explored for several decades but interest in conjugated polymers, attractive in view of their robustness and processability, has mushroomed since 1989 when Richard Friend *et al*. generated yellow–green light from a poly(phenylene vinylene) (PPV) light-emitting diode (Burroughes *et al.*, 1990). The process relies on charge conduction *via* delocalised p-electrons along a molecular framework of alternating single and multiple bonds. PPV, formed by thermal conversion from precursors, offers little scope for control of the chain microstructure and alignment. By contrast, a recently developed alternative, poly(9,9-dioctylfluorene) (PFO), a conjugated liquid-crystalline polymer made up of an aromatic backbone of repeated linked benzene rings with long aliphatic side-chains, has a structure offering some ability for control through thermal processing. It emits light in the blue region of the spectrum. Grazing angle diffraction techniques were employed to probe the surface and bulk regions of PFO samples. Two scattering geometries were employed which are sensitive to (A) surface normal and (B) in-plane correlations. PFO samples annealed at 130°C and 180–200°C, known from calorimetric measurements to have different liquid crystalline states, were investigated, as shown in Fig. 20. The data show that the buried interface with the substrate defines a unique orientation in the polymer film and that the two phases both show ordering normal to the interface whereas the crystalline phase alone displays in-plane ordering (Kawana *et al*., 2001). Grazing-incidence studies of the surface ordering, which is particularly important given the role of the interface in potential electronic applications, are in progress.

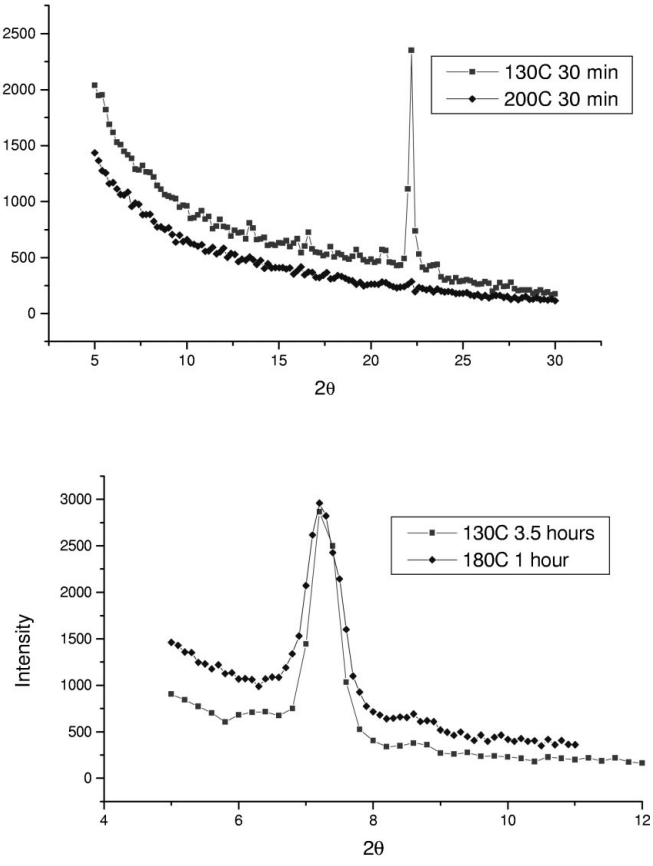

Figure 20
Grazing-incidence scans for samples in the two liquid-crystalline phases of PFO. The upper and lower diagrams relate to surface normal and in-plane scans, respectively. The higher-temperature phase shows nematic liquid-crystalline ordering whereas the lower-temperature phase is crystalline.

4. Summary

In the first 3.5 years of operation, the instrumental developments described in this paper have ensured that the XMaS beamline is a

unique, internationally competitive facility. The results in section 3 above are merely a representative selection of the work on the science performed and were chosen to illustrate the use of the diverse instrumental features of the beamline. Further details of those studies can be obtained from the individual authors and further information about the beamline and its instrumentation can be found at the website *www.esrf.fr/exp_facilities/BM28/xmas.html*.

We thank especially our users from Daresbury Laboratory and the Universities of Liverpool, York and Cardiff for permission to present their research and to reproduce Figs. 9 (Steve Collins and David Laundy), 12 (Jon Goff), 19 (Helen Laidler) and 20 (Emyr MacDonald). We are very grateful to the following colleagues who assisted in the conception and construction of the XMaS beamline; S. Beaufoy, E. M. Forgan , J. B. Forsyth, M. Hart and C. A. Norris. We thank the Engineering and Physical Sciences Research Council for their financial support of the construction and operation of this beamline. The advice of EPSRC, ESRF staff and other scientific colleagues is gratefully acknowledged. We are particularly grateful to S. Pujol of the ILL Cryogenic laboratory for making the low-temperature cryostat, and for A. Freund and the ESRF Optics group staff for the monochromator first crystal design and fabrication.

References

Burroughes, J. H., Bradley, D. D. C., Brown, A. R., Marks, R. N., Mackay, K., Friend, R. H., Burn, P. L. & Holmes, A. B. (1990). *Nature (London)*, **347,** 539.

Collins, S. P., Laundy, D. & Rollason, A. J. (1992). *Philos. Mag.* B**65**, 37–46

Czopnik, A., Iliew, N., Stalinski, B., Madge, H., Bozan, C. & Pott, R. (1985). *Physica B*, **130**, 262.

Goff, J. P., Sarthour, R. S., McMorrow, D. F., Yakhou, F., Stunault, A., Vigliante, A., Ward, R. C. C. & Wells, M. R. (1999). *J. Phys. Condens. Matter*, **11**, L139–L146.

Hannon, J. P., Trammell, G. T., Blume, M. & Gibbs, D. (1988). *Phys. Rev. Lett.* **61**, 1245.

Holloway, L. & Laidler, H. (2000). *J. Appl. Phys.* **87**, 5690.

Holloway, L., Laidler, H., Telling, N. D. & Wu, S. Z., (2001). *J. Appl. Phys.* In the press.

Kawana, S., Durrell, M., Lu, J., Macdonald, J. E., Grell, M., Bradley, D. D. C., Jukes, P., Jones, E. R. A. L. & Bennett, S. L. (2001). *Polymer*. Submitted.

Laundy, D., Brown, S., Cooper, M. J., Paul, D. F., Bowyer, D., Thompson, P., Stirling, W. G. & Forsyth, J. B. (1998). *J. Synchrotron Rad*. **5**, 1235–1239.

Lee, S., Goff, J. P., Ward, R. C. C., Wells, M. R. & Brown, S. (2001). To be published.

Longfield, M. J., Stirling, W. G., Lidstrom, E., Mannix, D., Lander, G. H., Stunault, A., McIntyre, G. J., Mattenberger, K. & Vogt, O. (2001). *Phys Rev B*, **63**, 134401–134408.

Macdonald, J. E., Durell, M., Wehrum, A., Jukes, P., Jones, R. A. L., Walker, C. J. & Brown, S. (2001). *Europhys. Lett.* In the press.

Moller, F. A., Kintrup, J., Lachenwitzer, A., Magnussen, O. M. & Behm, R.J., (1996). *Phys. Rev. B*, **56**, 12506.

Morin, P., Giraud, M., Burlet, P. & Czopnik, A. (1987). *JMMM*, **68**, 107. Nicklin, C., Norris, C., Alcock, S., Brust, M. & Brown, S. (2001). XMaS Newsletter.

Paul, D. F., Cooper, M. J. & Stirling, W. G. (1995). *Rev. Sci. Instrum.* **66**, 1741–1745.

Rakhecha, V. C., Chakravarthy, R. & Sayta Murthy, N. S. (1974). *Proceedings of the Conference on Neutron Scattering*, Gatlingburg, TN, USA, **2**, 638.

Wang, J., Ocko, B. M., Davenport, A. J. & Isaacs, H. S. (1992). *Phys. Rev B*, **46**, 10321.

Weller, D. & Doerner, M. F. (2000). *Annu. Rev. Mater. Sci.* **30**, 611.

Zukowski, E., Andrejczuk, A., Cooper, M. J., Dixon, M. A. G., Gardelis, S., Lawson, P. K., Buslaps, T., Kaprzyk, Neumann, K.-U. & Ziebeck, K. R. A. (1997). *J. Phys. Condens. Matter*, **9,** 10093–11005.

Zukowski, E., Cooper, M. J., Armstrong, R., Ito, M., Collins, S. P., Laundy, D. & Andrejczuk, J. (1992). *X-ray Sci. Technol.* **3**, 300–310.